ARTICLE

A sustainable mesoporous palladium-alumina catalyst for efficient hydrogen release from N-heterocyclic liquid organic hydrogen carriers

Jinho Oh [1,4], Hari Babu Bathula [1,2,4], Ji Hoon Park [3] & Young-Woong Suh [1,2]

Liquid organic hydrogen carriers (LOHC) are interesting hydrogen vectors which can exploit existing infrastructure. Specifically, N-heterocyclic compounds are attractive due to lower dehydrogenation enthalpy than homocyclic ones and demand a viable palladium catalyst to guarantee high dehydrogenation activity at low temperatures and stability in recycle runs. Here, we employ one-pot solvent deficient precipitation yielding a mesoporous palladium-alumina. The prepared catalyst system offers higher hydrogen release capability by 20% than conventional palladium/γ-Al$_2$O$_3$ in the dehydrogenation of four different N-heterocyclic compounds at or below 250 °C. Futhermore, it shows negligible activity loss up to five consecutive runs for perhydro 2-(n-methylbenzyl)pyridine and perhydro 2-methylindole. Such dehydrogenation performance is caused by the solvent deficient environment that restricts palladium mobility by contiguous alumina particles and produces well-dispersed palladium phase with a higher density of (111) plane. Therefore, the reported synthesis method may contribute to the production of innovative dehydrogenation catalysts for LOHC compounds.

[1] Department of Chemical Engineering, Hanyang University, Wangsimni-ro 222, Seongdong-gu, Seoul 04763, Republic of Korea. [2] Research Institute of Industrial Science, Hanyang University, Wangsimni-ro 222, Seongdong-gu, Seoul 04763, Republic of Korea. [3] Carbon Resources Institute, Korea Research Institute of Chemical Technology, Gajeong-ro 141, Yuseong-gu, Daejeon 34114, Republic of Korea. [4] The authors contributed equally: Jinho Oh, Hari Babu Bathula. Correspondence and requests for materials should be addressed to Y.-W.S. (email: ywsuh@hanyang.ac.kr)

Hydrogen as a future energy carrier is the most efficient, nontoxic and environmentally friendly fuel, because water is the only by-product in the conversion into energy through combustion or fuel cells, thus eliminating emission of greenhouse gases[1–4]. Yet, the realization of a hydrogen economy highly relies on how to overcome various storage and transportation issues caused by H_2's low volumetric density[3,5]. Of all different technologies, chemical hydrogen storage by liquid organic hydrogen carrier (LOHC) has been recently recognized as the most promising solution[6–9]. The LOHC concept is based on a pair of high boiling-point organic compounds that can be catalytically converted from an energy-lean to energy-rich form by hydrogenation and vice versa by dehydrogenation[6,10–12]. Among LOHC systems available in the literature[1,4,9,12–16], homocyclic compounds offer an advantage due to low cost and high compatibility with the existing infrastructures, but suffer significantly from a high heat of dehydrogenation[17,18]. Thus, theoretical and experimental studies validated that the incorporation of heteroatoms in the chemical structure of homocyclic LOHC compounds reduced the enthalpy of dehydrogenation and therefore favored H_2 release at low temperatures[19–21]. The representative example is a pair of N-ethylcarbazole (H_0-NEC) and its corresponding perhydro product (H_{12}-NEC), which has attracted a lot of attention from an academia and industry[3,5,9–11,13,20]. However, the downside of this pair for practical approach could be the thermal stability and physical state of H_0-NEC (i.e. solid at room temperature). Recent works hence demonstrated a potential of quinaldine[22], indole derivatives[23,24], and pyridine derivative[6,25] as alternative LOHC material.

Even though the dehydrogenation of these N-heterocyclic LOHC compounds is thermodynamically favorable compared to homocyclic compounds, an active and stable catalyst is still challenging because a relatively high reaction temperature is required for fast H_2 release. In most of the previous works Pd catalysts are known to work efficiently though Pt catalysts are also reported. Particularly, Smith's[3,5] and Wasserscheid's[26,27] groups investigated various supported Pd catalysts in the dehydrogenation of H_{12}-NEC, where the common support was alumina. Also, a 5 wt% Pd/Al_2O_3 catalyst was applied for the dehydrogenation of perhydro alkylindoles[23,24]. In case of perhydro 2-(n-methylbenzyl)pyridine (H_{12}-MBP) we documented last year, supported Pd catalysts proved to be more active than Pt analogues[6]. Aside from the dehydrogenation efficiency, catalyst stability is an important issue due to process operation at high temperatures above 200 °C, in which the metal-support interaction generally determines the lifetime of a tested dehydrogenation catalyst. For instance, our recent report revealed that a carbon-coated alumina supported Pd catalyst showed the enhanced stability than Pd/C and Pd/Al_2O_3, because the heterogeneity of support surface prevented Pd nanoparticles from sintering into larger sizes during the reaction[25]. Nevertheless, this strategic approach via carbon coating using an aqueous glycerol solution is rather complex and the optimal carbon content depends on the textural and acidic properties of the fresh alumina used for carbon coating.

Among numerous synthesis methods for supported Pd catalyst system, we paid much attention to a one-pot solvent deficient precipitation (SDP) method. Woodfield and colleagues[28,29] proposed the original synthesis method and focused on a variety of single and mixed metal oxides, particularly, alumina[29]. The synthesis typically involves only two steps: the metal salt is first mixed with a simple base in a solid state to yield an intermediate hydroxide product (e.g. metal hydroxide or metal oxide hydroxide) that further undergoes dehydration for the formation of intermediate nanoparticles, followed by the high-temperature calcination for crystallization and meso-structuring. This method is not only simple and cost effective, but also produces metal oxide particles with the high surface area and mesoporosity even though surfactant or structure directing agent is absent. This uniqueness would promise to yield an active and stable supported Pd catalyst, as demonstrated in iron Fischer–Tropsch catalysts[30–32] and nickel methane reforming catalysts[33,34].

Herein, we report the dehydrogenation activity and stability of Pd-Al_2O_3 catalyst prepared by the SDP method. The prepared catalyst system show mesoporosity, thus labelled as MPdA where M stands for mesoporosity, and retain Pd nanoparticles that are mainly composed of Pd(111) plane. In the dehydrogenation of perhydro 2-(n-methylbenzyl)pyridine MPdA offers improved H_2 release capability compared to Pd counterparts prepared by conventional impregnation, which is further demonstrated in four different N-heterocyclic compounds. Moreover, the dehydrogenation activity of MPdA is maintained up to five consecutive recycle runs because of lessened sintering of Pd particles. These features in catalyst property and performance stem from the generation of solvent deficient environment in the SDP synthesis, which is examined by characterization of uncalcined precursor materials.
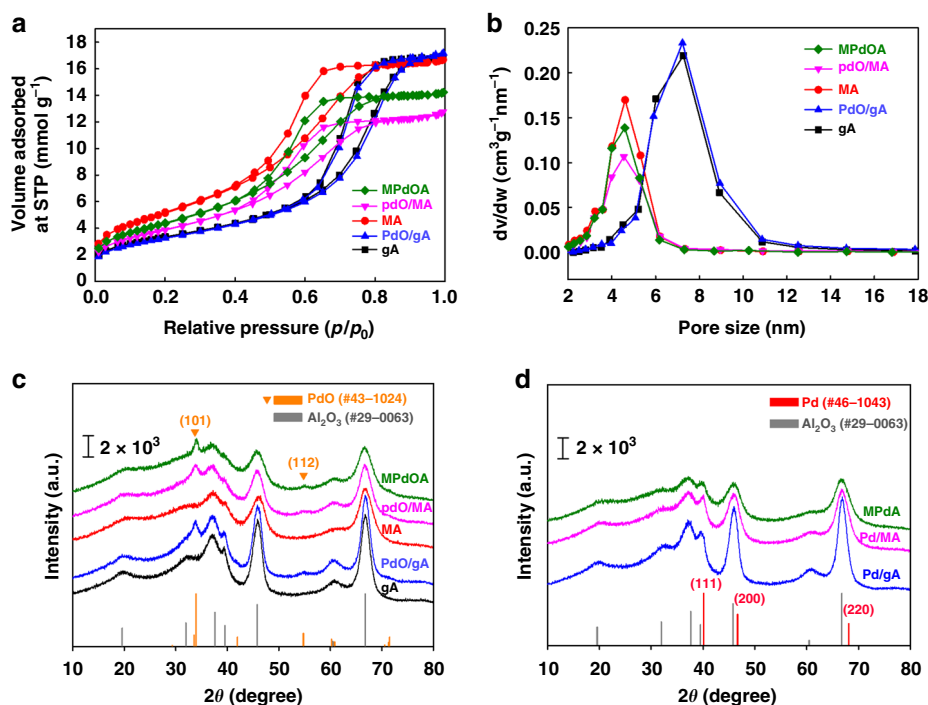
Results

Synthesis and properties of mesoporous PdO–Al_2O_3 material.
The original synthesis recipe was amended for a MPdA catalyst of 1 wt% Pd loading, which would expect to form a homogeneous Pd–Al solid solution (Supplementary Movie 1). First, palladium nitrate (Pd(NO_3)$_2$·H_2O), aluminum nitrate (Al(NO_3)$_3$·9H_2O) and ammonium bicarbonate (NH_4HCO_3) of desired amounts were mixed together in a mortar and grounded thoroughly by a pestle at room temperature, where no additional solvents including water were added for dissolving the solid salts. As depicted in Supplementary Fig. 1, the hand-grinding initially formed a brownish liquid as hydrated water molecules were released from the metal salts and CO_2 bubbles were from NH_4HCO_3. It continued until complete Al precipitation that was witnessed by negligible formation of bubbles. This process took about 20 min. Then, the resulting wet solid was directly calcined at 600 °C for 5 h with a ramping rate of 2 °C min^{-1} to ensure uniform pore development and attain better homogeneity by lowering a dehydration rate and avoiding rapid grain growth. The calcined samples were subjected to H_2 reduction at 350 °C for 3 h prior to the activity test. Note that the optimal Pd loading and calcination temperature were determined through preliminary tests for the dehydrogenation of H_{12}-MBP (Supplementary Table 1): (a) when the Pd loading varied from 1 to 5 wt% with an interval of 2 wt%, the H_2 yield (calculated from GC results) and H_2 volume (measured by a gas burette) were the highest at the Pd loading of 1 wt % and (b) when the calcination temperature varied from 400 to 700 °C with an interval of 100 °C, the dehydrogenation efficiency was the maximum for the MPdA sample calcined at 600 °C. The measured catalytic activities agreed well with the results of Pd particle size and Pd dispersion measured by CO pulse chemisorption experiments.

First of all, the calcined samples were characterized by N_2 physisorption, as listed in Table 1. The non-reduced MPdOA follows the type IV isotherm with a composite of H2 and H3 hysteresis loops representing the presence of mesopores (the most probable pore diameter of 4.1 nm calculated from the desorption branch) with ink-bottle or channel-like pore connectivity (Fig. 1a, b), which is consistent with the characteristics of the previous materials prepared by the solvent deficient precipitation method[29]. The very similar isotherms were taken for MA (mesoporous Al_2O_3 prepared without Pd source using the same procedure as MPdOA) and 1 wt% PdO/MA (prepared by incipient wetness impregnation of Pd source onto MA) samples.

Table 1 Properties of the calcined and reduced samples (1 wt% Pd loading) prepared in this work

Sample	BET surface area ($m^2\,g^{-1}$)	Pore volume/diameter[a] ($cm^3\,g^{-1}$/nm)	Pd particle size[b] (nm)	Avg. Pd particle size[c] (nm)	H_2 consumption[d] ($\mu mol\,g^{-1}$)
gA	271	0.59 / 6.4	–	–	–
MA	420	0.57 / 4.1	–	–	–
Pd/gA	264	0.59 / 6.5	4.4 (25.1%)	5.3 (11.5)	1.61
Pd/MA	316	0.43 / 4.1	3.3 (34.0%)	4.4 (9.6)	1.17
MPdA	359	0.49 / 4.1	2.6 (42.4%)	3.4 (4.0)	0.61

[a]calculated from the desorption branch of BET isotherm
[b]measured by CO pulse chemisorption experiments, in which the value in parenthesis represents the Pd dispersion that gives the Pd surface area of 112 (Pd/gA), 152 (Pd/MA), and 190 (MPdA) $m^2\,g^{-1}$
[c]estimated in TEM images, in which the value in parenthesis represents the average Pd particle size in spent catalyst samples
[d]measured by H_2-TPR experiments

Fig. 1 BET and XRD results of the samples prepared in this work. **a** N_2 adsorption-desorption isotherms of supported PdO samples and support materials. **b** Their pore size distribution curves. **c** Their XRD patterns. **d** XRD patterns of supported Pd catalyst samples reduced at 350 °C for 3 h

The BET surface area and pore volume were lower for MPdOA and PdO/MA compared to MA due to the existence of PdO particles that was evidenced by the standard reflections of PdO (101) and (112) planes (JCPDS #43-1024) in Fig. 1c. Importantly, MPdOA was more porous than PdO/MA, possibly resulting from a homogeneous solid solution made by the one-pot method, although the XRD patterns of the two samples appeared very similar. In contrast, 1 wt% PdO supported onto commercially available γ-Al$_2$O$_3$ (hereafter abbreviated as gA) showed the low specific surface area of 264 $m^2\,g^{-1}$ even though the pore volume (0.59 $cm^3\,g^{-1}$) and diameter (6.5 nm) were larger compared to MPdOA and PdO/MA because of high crystallinity of γ phase in the parent alumina.

Dehydrogenation activity of mesoporous Pd-Al$_2$O$_3$ catalyst. The catalyst samples obtained after H_2 reduction under the identical condition were tested in the dehydrogenation of H_{12}-MBP for 4 h with the metal-to-reactant (M/R) ratio of 0.1 mol%, where H_2 volume was monitored by a gas burette. When the catalytic performance was first compared at 250 °C, the volume of

H_2 released was higher for MPdA (790 cm^3) than for Pd/MA and Pd/gA (Fig. 2a). MPdA also showed the higher 1st-order rate constant (0.031 $min^{-1}\,g_{cat}^{-1}$) and turnover frequency (98.9 min^{-1}) than Pd/MA and Pd/gA (Supplementary Table 2). Moreover, the volume of H_2 released was larger over MPdA under the identical condition than over the benchmark catalyst Pd/C (662 cm^3) reported in our previous work (Supplementary Table 3). The next comparison at 230 °C confirmed that MPdA (496 cm^3) was more active than Pd/MA and Pd/gA. This was also true in the activity tests at 270 °C. In terms of the dehydrogenation efficiency, MPdA exhibited the higher values at all the reaction temperatures (Table 2). From the Arrhenius plot, the activation energy (E_a) value of MPdA was much smaller (49.7 $kJ\,mol^{-1}$) compared to those of the other impregnated catalysts Pd/MA (80.6 $kJ\,mol^{-1}$) and Pd/gA (84.4 $kJ\,mol^{-1}$), indicating that MPdA is the best among the studied catalysts.

The volumetric measurement results matched well with those calculated by analyzing the composition of the product mixtures obtained after the 4 h reaction using a gas chromatograph (GC), where the measurement errors ranged within 1–1.5% (Table 2).
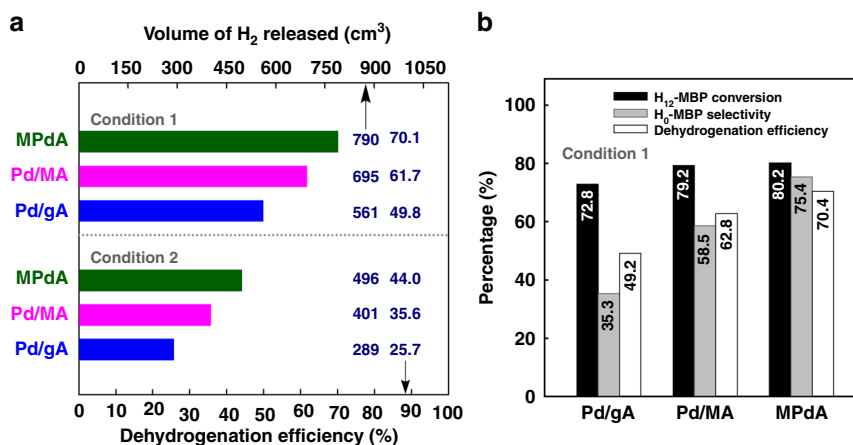
Fig. 2 Catalytic activities of MPdA, Pd/MA and Pd/gA in the dehydrogenation of H_{12}-MBP for 4 h. **a** Dehydrogenation efficiency and volume of H_2 released under different reaction conditions: (1) 250 °C and 0.1 mol% M/R and (2) 230 °C and 0.1 mol% M/R. **b** GC results of the product mixtures obtained under the condition 1

Table 2 Activity results and kinetic parameters in the dehydrogenation of H_{12}-MBP with 0.1 mol% M/R

Catalyst	Temp. (°C)	H_{12}-MBP conversion[a] (mol%)	H_0-MBP selectivity[a] (mol%)	H_2 yield[a] (mol%)	Dehydrogenation efficiency[b,c] (mol%)	Rate constant (min^{-1})	E_a (kJ mol^{-1})
MPdA	230	56.8	55.7	44.2	44.0 (496, 2.71)	0.020	49.7
MPdA	250	80.2	75.4	70.4	70.1 (790, 4.31)	0.031	
MPdA	270	98.9	98.2	98.0	99.0 (1115, 6.09)	0.049	
Pd/MA	230	52.4	35.2	35.4	35.6 (401, 2.19)	0.009	80.6
Pd/MA	250	79.2	58.5	62.8	61.7 (695, 3.79)	0.020	
Pd/MA	270	95.2	98.0	94.3	94.2 (1061, 5.79)	0.038	
Pd/gA	230	41.7	23.7	25.8	25.7 (289, 1.58)	0.007	84.4
Pd/gA	250	72.8	35.3	49.2	49.8 (561, 3.06)	0.014	
Pd/gA	270	91.8	98.4	91.1	91.1 (1026, 5.60)	0.031	

[a]calculated from GC results
[b]calculated by dividing the volume (unit: cm^3) of H_2 released for 4 h (the first value in parenthesis; measured in time-dependent H_2 release curve shown in Supplementary Fig. 2) into the H_2 volume released by complete dehydrogenation of H_{12}-MBP (1126.4 cm^3)
[c]the second value in parenthesis indicates the H_2 release capacity (unit: wt%) based on the theoretical H_2 storage capacity of H_{12}-MBP (6.15 wt%)

For the product mixtures obtained at 250 °C, GC analysis revealed that the selectivity to the full dehydrogenation product H_0-MBP was 2-fold higher over MPdA than over Pd/gA whereas the difference in the conversion of H_{12}-MBP was merely 7.4% (Fig. 2b). This was also found for Pd/MA, even if the difference was smaller compared to Pd/gA.

Since it was believed that a higher selectivity to H_0-MBP greatly contributed to the improved dehydrogenation efficiency of MPdA, the activity test was conducted for a different period of 0.5, 1 or 4 h at 250 °C and 0.4 mol% M/R. In gas chromatogram of the product mixture conducted over MPdA for 0.5 h, huge GC peaks corresponding to H_0-MBP were detected along with those of unconverted H_{12}-MBP (Fig. 3a), resulting in the H_{12}-MBP conversion of 41.9% and the outstanding H_0-MBP selectivity of 96.8%. As the reaction over MPdA progressed up to 4 h, the H_{12}-MBP conversion increased to ca. 94% with the H_0-MBP selectivity maintaining near 97%. In sharp contrast, GC peaks of the reaction intermediate H_6-MBP were obviously seen for all product mixtures obtained over Pd/gA (Fig. 3b). The calculation showed that the conversion of H_{12}-MBP increased from 30.9 to 83.2% and the selectivity to H_0-MBP also did from 36.7 to 64.9% as the reaction progressed to 4 h. This suggests that MPdA catalyst is selective in the dehydrogenation of H_{12}-MBP (time-dependent H_2 release curve shown in Supplementary Fig. 2).

The dehydrogenation efficiency could be enhanced to over 90% by increasing the temperature to 270 °C at 0.1 mol% M/R

(Table 2) or by adding more catalyst up to 0.4 mol% M/R at 250 °C (92.4%). Note that the dehydrogenation efficiency approached nearly 99% by the former approach, which is attributed to lower dehydrogenation enthalpy values of N-heterocyclic compounds (i.e., H_{12}-MBP (67.3 kJ/mol$_{H2}$)[6], H_{12}-NEC (55 kJ/mol$_{H2}$)[35], octahydroindole (57.5 kJ/mol$_{H2}$)[36], decahydroquinoline (61.9 kJ/mol$_{H2}$)[37], and perhydro 2-methyl-6-(n-methylbenzyl)pyridine (66.7 kJ/mol$_{H2}$)[6] compared to homo-cyclic counterparts (i.e. H_{12}-benzyl toluene (71 kJ/mol$_{H2}$)[6,35] that is a counterpart of H_{12}-MBP and decaline (63.9 kJ/mol$_{H2}$)[37] that is a counterpart of decahydroquinoline).

Furthermore, the dehydrogenation activities of MPdA and Pd/gA were compared for different N-heterocyclic compounds (Fig. 4 and Supplementary Fig. 3). When octahydroindole (i) was tested at 180 °C due to the low boiling point of 222.7 °C, MPdA exhibited the larger volume of released H_2 by 10.5% than Pd/gA. Also, the similar difference of about 12% was found for decahydroquinoline (ii) and for perhydro 2-methyl-6-(n-methylbenzyl)pyridine (iii of which the theoretical H_2 storage capacity is 5.8 wt%[6]) at 230 °C. When the last comparison was done for H_{12}-NEC (iv), the dehydrogenation activity of MPdA at 230 °C was higher by 20.6% than that of Pd/gA. These results suggest that the catalyst MPdA prepared in this work has great potential in the dehydrogenation of various N-heterocyclic compounds.

To demonstrate the effectiveness of MPdA catalyst, the powder sample was pressurized with a PIKE CrushIR Hydraulic Press at
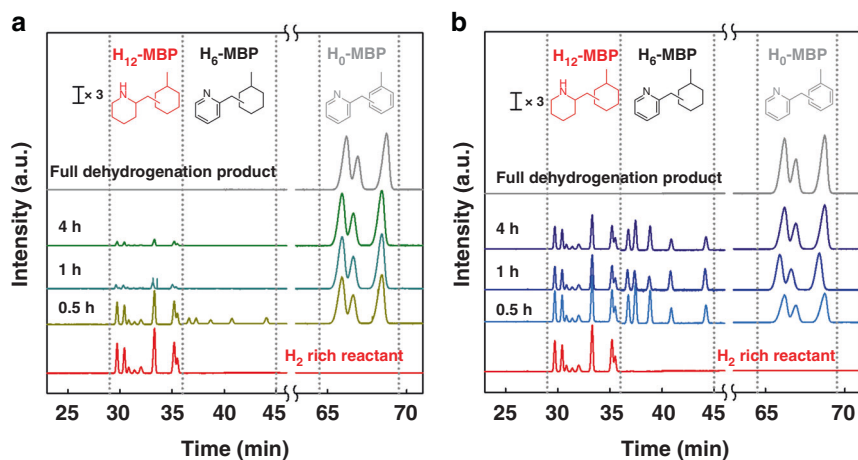
Fig. 3 GC chromatograms of the product mixtures obtained at different reaction periods in the dehydrogenation of H_{12}-MBP. **a** MPdA. **b** Pd/gA. Reaction condition: 250 C and 0.4 mol% M/R
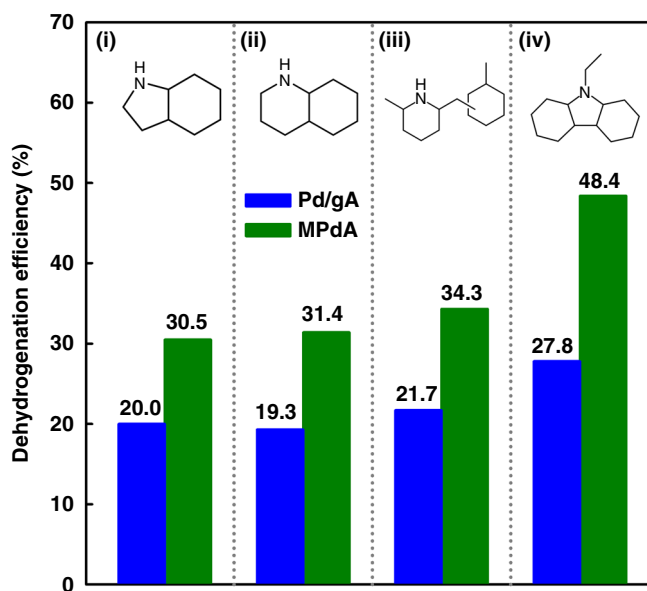

Fig. 4 Activity comparison of MPdA and Pd/gA catalysts. The tested compounds are octahydroindole (**i**), decahydroquinoline (**ii**), perhydro 2-methyl-6-(n-methylbenzyl)pyridine (**iii**), and H_{12}-NEC (**iv**). While the M/R value was fixed at 0.1 mol%, the activity tests were conducted at 230 °C for all compounds except for the first compound which was conducted at 180 °C

0.5 US tons using an in-house die to give a pellet of 3 mm diameter and 5 mm length. As shown in Supplementary Fig. 4, the pellet-type MPdA exhibited the similar H_2 evolution curve to the corresponding powder while the dehydrogenation rate in the initial run was a little low. Furthermore, the analogous H_2 evolution results were obtained in the next three consecutive cycles over the pellet-type MPdA catalyst. It is worth noting here that the low H_2 evolution rate at the initial stage of dehydrogenation is possibly due to diffusion limitation resulting from the pellet structure. When the product mixture was analyzed by GC, the H_2 yield was estimated to be 66.6% that is lower by only 4% than the powder sample. This result guarantees the viability of one-pot solvent deficient precipitation method for the practical application albeit optimization study needs to be done in near future.

Pd characteristics of mesoporous Pd–Al$_2$O$_3$ catalyst. Since we could not distinguish the reflections of metallic Pd in XRD patterns of the reduced samples due to overlapping with the reflections of alumina (Fig. 1d), CO pulse chemisorption experiments were conducted to estimate the size and dispersion of Pd particles. They unveiled that MPdA retained the smallest Pd particles (Pd size = ca. 2.6 nm, Pd dispersion = 42% and Pd surface area = 190 m^2 g^{-1}) than the other catalyst samples (Table 1). This finding was supported by high angle annular dark field scanning transmission electron microscopy (HAADF-STEM) images of fresh samples. When the average sizes were calculated from the particle size distribution charts (Supplementary Fig. 5), the average size of Pd particles increased in the following order: MPdA (3.4 nm) <mPd/MA (4.4 nm) m)Pd/gA (5.3 nm) (Supplementary Fig. 6a).

Furthermore, the samples were characterized by H$_2$-TPR experiments (Fig. 5a). For general Al$_2$O$_3$-supported Pd catalysts, a negative peak below 130 °C was reported to correspond to the decomposition of palladium hydride species formed by PdO reduction and subsequent H$_2$ storage around room temperature, where the intensity and position of this negative peak depend on the size of supported Pd metal particles[38–40]. In the samples studied herein, a negative peak of MPdA was smaller (volume of H$_2$ consumed = 0.61 μmol g^{-1}) and positioned at a higher temperature of 113 °C in comparison with Pd/MA and Pd/gA (Table 1). This indicates the existence of smaller-sized Pd particles in MPdA, which is in good accordance with CO pulse chemisorption results and HAADF-STEM images. The finding is attributed to the solvent deficient environment generated in the synthesis that inhibits the migration of reagent materials and subsequently the over growth of nanoparticles[30,41]. Therefore, we believed that the higher dehydrogenation performance of MPdA was attributed to the higher surface area and greater dispersion of Pd particles.

Besides, CO-chemisorbed DRIFT spectrum of MPdA showed very distinguishable spectral features from those of Pd/MA and Pd/gA[42]. According to the report of Zhu et al.[42], five IR bands were assigned as shown in Fig. 5b; linearly bound CO bands (A$_1$ and A$_2$) above 2000 cm^{-1} and multiply bound CO bands (B, C, and D) below 2000 cm^{-1}. In the former region MPdA exhibited peak maximum at 2064 cm^{-1}, in contrast to Pd/MA and Pd/gA showing the band at 2086 cm^{-1} that represents linearly bound CO on defects (mainly, corners) of Pd crystallites[42–44]. Hicks et al. assigned the band at 2064 cm^{-1} to CO adsorption on well dispersed but not crystalline Pd[45], while Lear et al. reported that
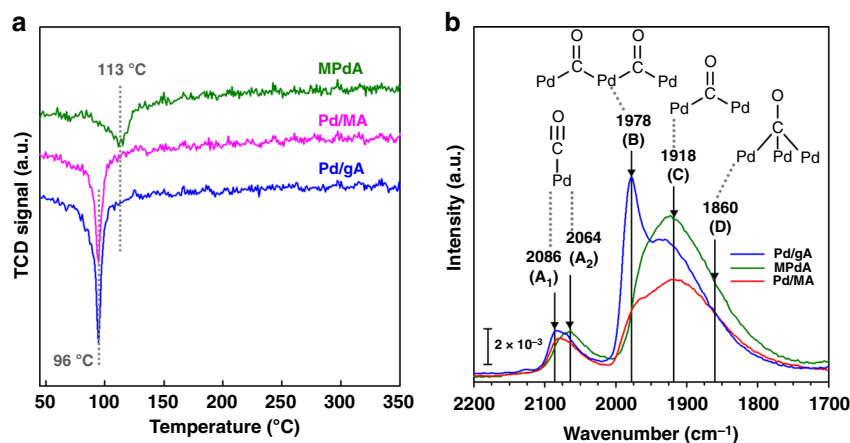
Fig. 5 Catalyst characteristics of MPdA compared to Pd/MA and Pd/gA. **a** H$_2$-TPR profiles. **b** CO-chemisorbed DRIFT spectra
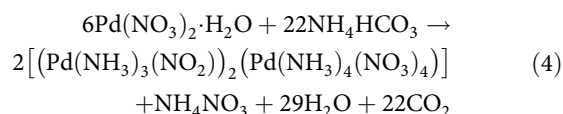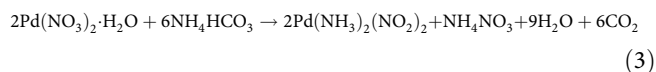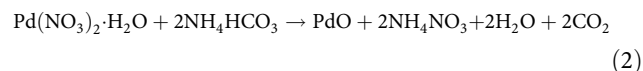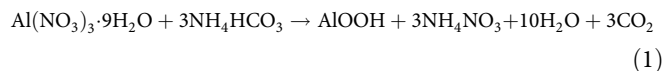
linearly bound CO on Pd particles' edge sites related with (111) facet was responsible for this band[46]. In the latter region MPdA exhibited stronger bands at 1918 and 1860 cm^{-1} than the impregnated counterparts, where these bands are attributed to isolated-bridged and tri-coordinated CO adsorption on Pd(111) facet. In contrast, the impregnated catalysts than MPdA displayed a stronger band at 1978 cm^{-1} that is ascribed to compressed-bridged CO adsorbed on structurally open crystal planes such as (100) or (110)[47,48]. It is worth noting here that the dehydrogenation reaction proceeds dominantly over thermodynamically stable Pd(111) facet of Pd nanoparticles supported on Al$_2$O$_3$ due to the closed-packing of Pd atoms that favor the preferred adsorption geometry of N-heterocyclic LOHC compounds by keeping H atoms on the LOHC molecule and Pd atoms in close proximity and eventually lead to the faster dehydrogenation compared to other Pd surfaces of less packing such as Pd(100) and Pd(110)[3,5,26,27]. When the relative intensity of CO adsorption bands was calculated in a manner that the intensity sum of Pd(111)-related bands C and D is normalized by the intensity of non Pd(111)-related band B (Supplementary Table 4), MPdA (3.8) showed a higher value than Pd/MA (2.4) and Pd/gA (1.0). This suggests that MPdA is mainly composed of well dispersed Pd phase with a higher density of (111) facet that is preferentially exposed to the reaction mixture, which explains its improved dehydrogenation ability.

Recyclability of mesoporous Pd–Al$_2$O$_3$ catalyst. In hydrogen release from H$_{12}$-MBP, the catalyst stability was verified at 250 °C and 0.4 mol% M/R in five consecutive runs. As noted in Fig. 6a (GC results in Supplementary Table 5), the dehydrogenation efficiencies of Pd/gA and Pd/MA continuously dropped to 49.0 and 69.1% in the fifth cycle, respectively, whereas the initial efficiency of MPdA (92.3%) was maintained during five runs. Furthermore, the catalyst durability in the dehydrogenation reaction was once again verified by selecting a recently demonstrated potential LOHC, i.e., perhydro 2-methylindole (H$_8$-MID) with a H$_2$ storage capacity of 5.76 wt%[24]. Figure 6b presents the much better stability of MPdA at 250 °C and 0.6 mol% M/R in which the H$_2$ release capacity was very stable at 5.70 wt% during five consecutive runs (GC results in Supplementary Table 6). It should be noted here that the different M/R values for H$_{12}$-MBP and H$_8$-MID were chosen in order to satisfy the liberated amount of H$_2$ required for the mobile applications, i.e., 5.5 wt% of gravimetric density recommended by the U.S. Department of Energy[4]. The improved stability resulted from the preservation of smaller Pd particles in MPdA (4.0 nm) compared to Pd/MA (9.6 nm) and Pd/gA (11.5 nm) that was acknowledged by HAADF-

STEM images of the spent samples after the dehydrogenation of H$_{12}$-MBP at 250 °C for 4 h (Supplementary Fig. 6b).

Feature of one-pot solvent deficient precipitation method. To understand the unique stability of MPdA, uncalcined precursors were characterized by XRD. According to the literature[30,32,41], the solid-state reaction between metal nitrate and NH$_4$HCO$_3$ forms a solvent deficient environment and then yields an intermediate hydroxide product (e.g. metal hydroxide or metal oxide hydroxide) and a byproduct ammonium nitrate (NH$_4$NO$_3$). The XRD pattern for a dried MA precursor (called "D precursor") confirmed the presence of NH$_4$NO$_3$ but did not show any reflections of Al phase due to strong diffraction peaks of the ammonium salt (Fig. 7a). Furthermore, the dried MA precursor was rinsed with H$_2$O and then dried again (called "DRD precursor"), of which the XRD pattern revealed a boehmite (AlOOH) phase (Fig. 7b) that is formed according to Eq. 1. Therefore, in the precursor stage boehmite aggregates are surrounded over ammonium nitrate acting as a spatial buffer or template[29,41]. Subsequent thermal calcination transforms boehmite to gamma-Al$_2$O$_3$ while producing mesopores by the decomposition of NH$_4$NO$_3$.

The diffraction peaks related to palladium were not detected in XRD patterns of two different precursors of MPdA due to the strong diffraction signals of NH$_4$NO$_3$ and AlOOH (Fig. 7a, b). Thus, Pd precursors were prepared using Pd(NO$_3$)$_2$·H$_2$O and NH$_4$HCO$_3$ without Al source. In XRD patterns of the D and DRD precursors of Pd, we observed three Pd-related species, such as PdO, Pd(NH$_3$)$_2$(NO$_2$)$_2$, and [(Pd(NO$_2$)(NH$_3$)$_3$)$_2$(Pd(NH$_3$)$_4$(NO$_3$)$_4$], (Fig. 7c) that are produced by chemical reactions, such as Eqs. 2–4 in the following:

$$Al(NO_3)_3 \cdot 9H_2O + 3NH_4HCO_3 \rightarrow AlOOH + 3NH_4NO_3 + 10H_2O + 3CO_2 \tag{1}$$

$$Pd(NO_3)_2 \cdot H_2O + 2NH_4HCO_3 \rightarrow PdO + 2NH_4NO_3 + 2H_2O + 2CO_2 \tag{2}$$

$$2Pd(NO_3)_2 \cdot H_2O + 6NH_4HCO_3 \rightarrow 2Pd(NH_3)_2(NO_2)_2 + NH_4NO_3 + 9H_2O + 6CO_2 \tag{3}$$

$$6Pd(NO_3)_2 \cdot H_2O + 22NH_4HCO_3 \rightarrow 2\left[\left(Pd(NH_3)_3(NO_2)\right)_2\left(Pd(NH_3)_4(NO_3)_4\right)\right] + NH_4NO_3 + 29H_2O + 22CO_2 \tag{4}$$

Therefore, these Pd species, boehmite and NH$_4$NO$_3$ are considered to be well mixed in MPdA precursor. After calcination
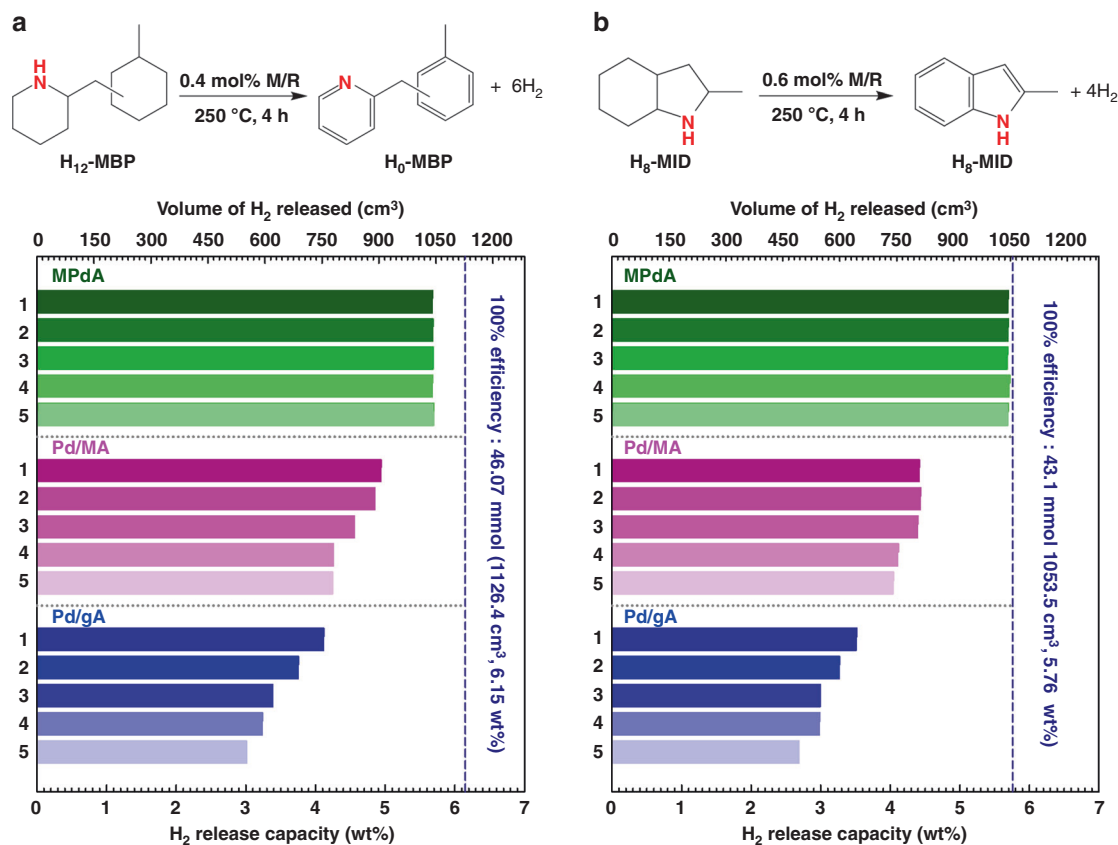
Fig. 6 Catalyst reuse of MPdA, Pd/MA and Pd/gA. **a** Dehydrogenation of H_{12}-MBP at 250 °C and 0.4 mol% M/R for 4 h. **b** Dehydrogenation of perhydro 2-methylindole (H_8-MID) at 250 °C and 0.6 mol% M/R for 4 h. The value in the left-hand side of each bar represents the number of catalyst use
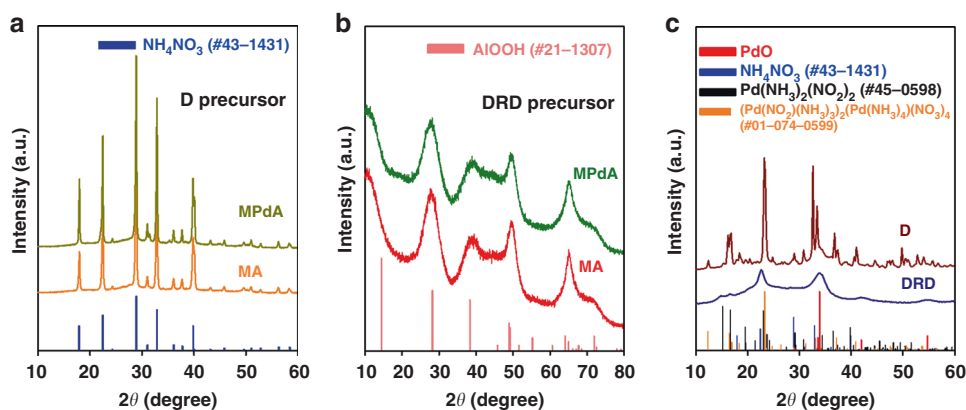

Fig. 7 XRD patterns of dried and dried-rinsed-dried precursors of MA, MPdA and palladium. **a** Dried (D) precursors of MA and MPdA. **b** Dried-rinsed-dried (DRD) precursors of MA and MPdA. **c** D and DRD precursors of palladium. D precursors were prepared by only drying at 105 °C for 14 h, and DRD precursors by rinsing D precursors with distilled water three times followed by drying again at 105 °C for 14 h

to bring about mesopore formation and phase transition, PdO particles would become protected by adjacent Al_2O_3 particles probably because the former particles of the extremely small population are located in the vicinity of the latter particles consisting of the mesopore wall, resulting in no appreciable difference in the pore diameters of MA and MPdOA (Fig. 1b). The high resolution transmission electron microscopy (HRTEM) images in Fig. 8a demonstrate that Pd particles are protected by Al_2O_3 layers in the fresh MPdA. In contrast, such kind of protection lacks in the HRTEM images of fresh Pd/MA (Fig. 8b) and Pd/gA (Fig. 8c). This difference is also visible for the spent MPdA, Pd/MA

and Pd/gA samples (Supplementary Fig. 7). Consequently, the dissimilar environment of Pd particles in MPdA, Pd/MA and Pd/gA will influence their surface mobility in the dehydrogenation reaction operated at high temperatures; compared to Pd/MA and Pd/gA, Pd particles are less mobile in MPdA by aid of neighboring alumina particles that can prevent the aggregation of Pd particles and hence keep the initial dehydrogenation activity of MPdA unchanged in the next four runs.

Moreover, we found an unexpected Pd character in the selected area electron diffraction (SAED) patterns obtained from the image of MPdA. In Pd/MA and Pd/gA, two diffraction patterns
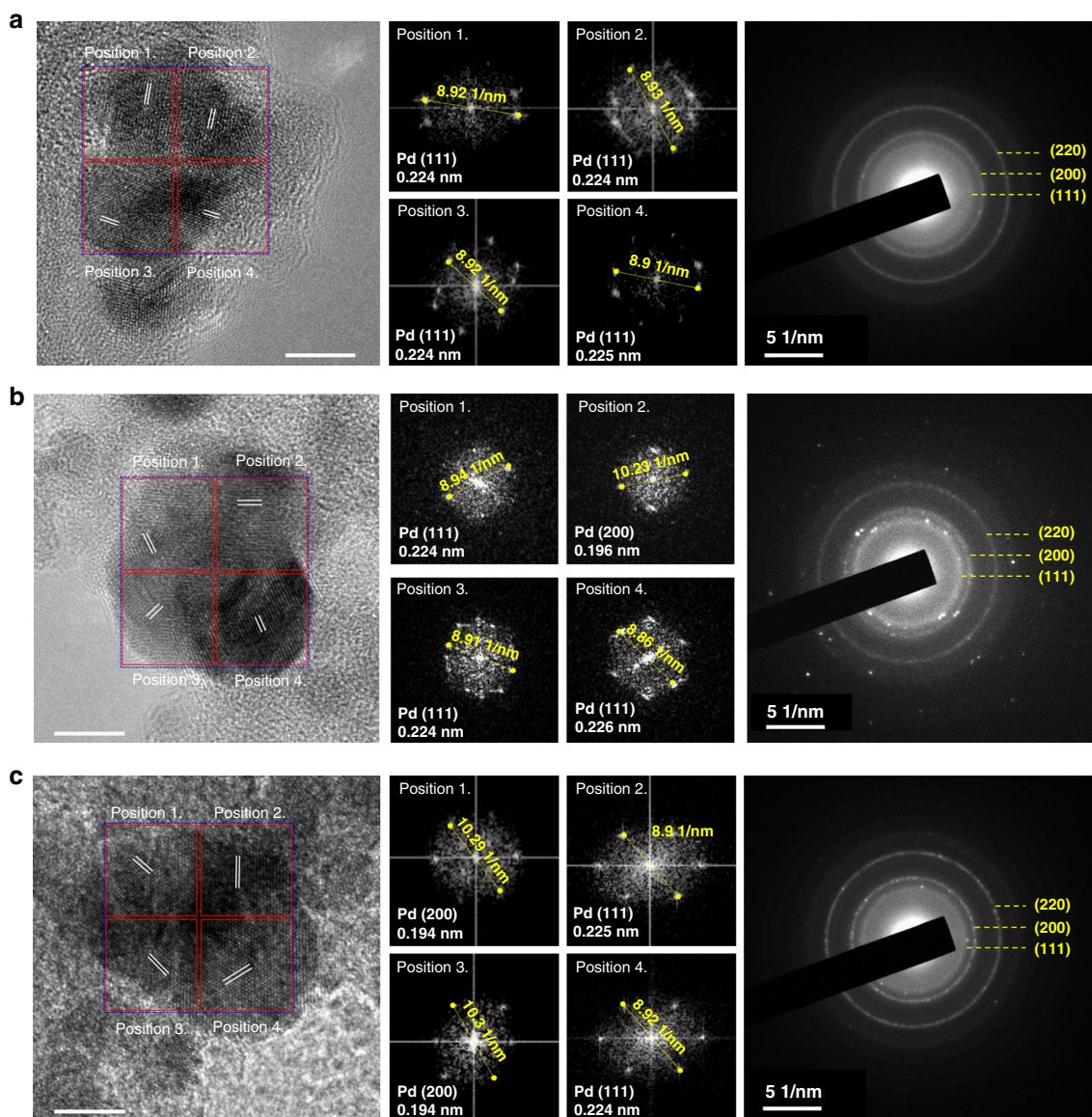
Fig. 8 HRTEM images and selected area electron diffraction patterns of fresh catalyst samples. **a** MPdA. **b** Pd/MA. **c** Pd/gA. (scale bar: 5 nm)

corresponding to Pd(111) and Pd(200) planes appeared whereas the SAED pattern of Pd(111) showing a *d*-spacing of 0.224 nm was captured all around the positions of MPdA. This indicates more presence of Pd(111) plane in MPdA. Additionally, the overall SAED patterns of MPdA, Pd/MA and Pd/gA (right-hand sided images in Fig. 8) revealed that bright small spots to make up the rings representing Pd(111), Pd(200) and Pd(220) planes were more evident in Pd/MA and Pd/gA than in MPdA, meaning that Pd particles are polycrystalline in the former samples whereas they are well dispersed in the latter sample. These SAED results further approve the finding of CO-chemisorbed DRIFT analysis that the population of Pd(111) plane decreases in the following order: MPdA PdPd/MA MAPd/gA.

Discussion

We demonstrate here a one-pot solvent deficient precipitation method for the preparation of mesoporous Pd-Al$_2$O$_3$ (MPdA) catalyst providing the improved H$_2$ release and outstanding durability in the dehydrogenation of *N*-heterocyclic compounds. Catalyst characterization works manifest the high dispersion of small Pd nanoparticles mainly composed of Pd(111) plane in the

fresh MPdA and the inhibited growth of Pd particles by Al$_2$O$_3$ neighbors in the consecutive reuse of MPdA. These unique properties are owing to the generation of solvent deficient environment in the synthesis, which not only constrains the nucleation and growth of nanoparticles but involves the participation of Pd and Al species in the construction of mesoporous wall. Consequently, the catalyst MPdA is believed to offer great potential in a variety of hydrogenation and dehydrogenation reactions, where Pd loading and calcination condition need to be specified for each reaction. In addition, the synthesis method reported herein can be applied potentially for other supported metal catalysts: for instance, we have very recently succeeded in preparing a mesoporous Pt–Al$_2$O$_3$ (MPtA) catalyst that shows extraordinary durability and highly greater hydrogenation and dehydrogenation performance for commercially available LOHC materials.

Methods

Synthesis of mesoporous Al$_2$O$_3$. Aluminum nitrate Al(NO$_3$)$_3$·9H$_2$O and ammonium bicarbonate NH$_4$HCO$_3$ with a molar ratio of 1:3 were mixed together in a mortar and grounded thoroughly by a pestle at room temperature, which proceeded during ca. 20 min. The resulting precursor was directly calcined at

600 °C for 5 h with a ramping rate of 2 °C min^{-1} to obtain a mesoporous Al_2O_3 (denoted as MA).

Synthesis of 1 wt% Pd supported on γ-Al_2O_3 or mesoporous Al_2O_3. A desired amount of $Pd(NO_3)_2.H_2O$ dissolved in an aqueous solution was impregnated onto γ-Al_2O_3 (STREM) or mesoporous alumina (MA). After drying at 105 °C in an oven, the final catalyst samples were obtained by calcination at 600 °C for 5 h with a ramping rate of 2 °C min^{-1} followed by H_2 reduction at 350 °C for 3 h with a ramping rate of 5 °C min^{-1}, yielding Pd/ γ-Al_2O_3 (Pd/gA) and Pd/MA.

Synthesis of mesoporous 1 wt% Pd–Al_2O_3. In a mortar, palladium nitrate Pd $(NO_3)_2·H_2O$ (78.459 mg), aluminum nitrate $Al(NO_3)_3·9H_2O$ (22.291 g), and ammonium bicarbonate NH_4HCO_3 (14.235 g) were mixed together and grounded thoroughly with a pestle at room temperature for ca. 20 min. The resulting material was subjected to the identical calcination as described above for MA synthesis, while the calcined sample was reduced under the condition identical for Pd/gA and Pd/MA. The prepared catalyst is denoted as MPdA.

Catalyst characterization. BET surface area of the sample (100 mg) was measured in a Micromeritics 3Flex after pretreatment at 200 °C for 2 h under vacuum. X-ray diffraction (XRD) analysis was conducted with a Rigaku miniFlex300 dif-fractometer using a Cu Kα source (30 kV and 10 mA), where all patterns were recorded in 2θ range 10–80° at a scan rate of 4° min^{-1} with a step of 0.02°. High resolution transmission electron microscopy (HRTEM) and high angle annular dark field scanning transmission electron microscopy (HAADF-STEM) images were taken in a JEOL JEM-2100F microscope with an acceleration voltage of 200 kV, where the specimen was prepared by dropping a catalyst powder in methanol onto a copper grid and vacuum drying at 60 °C. CO pulse chemisorption experiment was done in a BELCAT-B instrument (BEL Japan), where a sample of 50 mg was reduced at 350 °C for 3 h at a ramping rate of 5 °C min^{-1} in a 10% H_2/Ar flow of 30 cm^3 min^{-1}. After cooling to 30 °C in a He flow, 5% CO in He was repeatedly injected as pulses until the peak area became saturated. The amount of CO che-misorbed was determined by quantification of the integrated peak areas from the calibrated area obtained by injecting a 5% CO/He gas through a sample loop. From CO uptake data, the average size of Pd particles was calculated assuming a spherical geometry of Pd crystallites. Also, the percentage of exposed Pd atoms (i.e., Pd dispersion) was deduced from the assumption that the ratio CO/Pd is 1:1. In H_2 temperature-programmed reduction (H_2-TPR) experiments, a sample of 60 mg was pretreated under an argon flow at 500 °C for 1 h and then cooled down to room temperature. Then, the volume of H_2 consumed for supported Pd catalyst samples was measured on a Micromeritics AutoChemII 2910 instrument equipped with a thermal conductivity detector as the temperature increased up to 800 °C (10 °C min $^{-1}$) in a 10% H_2/Ar flow of 50 cm^3 min^{-1}. CO chemisorbed diffuse reflectance infrared fourier transform (DRIFT) spectra were taken in a Nicolet 6700 FT-IR installed with a Harrick Praying Mantis high-temperature reaction chamber. Prior to the measurement, a sample of 30 mg was reduced at 350 °C for 3 h in a 5% H_2/Ar flow of 100 cm^3 min^{-1}. The sample was cooled to 50 °C and the gas flow was then switched into argon for removal of physisorbed molecules. After Ar purge for 3 h, a background spectrum was taken. Then, the sample was exposed to 5% CO/Ar flow of 50 cm^3 min^{-1} for 30 min. Finally, a CO-chemisorbed DRIFT spectrum was acquired after evacuation for 30 min.

Catalytic activity test. A reduced catalyst sample was tested in the dehy-drogenation of H_{12}-MBP in a batch reactor (volume 90 cm^3) described previously[6,25]. In a typical experiment, H_{12}-MBP of 7.3 mmol was added dropwise to the catalyst pre-loaded at the bottom of the reactor vessel, where the catalyst weight varied to obtain a desired metal-to-reactant (M/R) ratio. Prior to the reaction, the reactor was purged with N_2 for 10 min to remove inner moisture and oxygen. Then, the reaction mixture was heated at 18 °C min^{-1} to a desired tem-perature using a commercial heat-transfer fluid, followed by the dehydrogenation reaction for a desired period. The volume of H_2 released during the reaction was monitored by the water volume displaced in a glass burette and measured with an accuracy of ±2 cm^3 (examined by repeating the experiment no less than three times under the identical condition). Notably, the close examination of gas and liquid products found no formation of other gases except H_2 (Supplementary Fig. 8) and no decomposition of the substrate in the liquid phase (Supplementary Fig. 9). After completion of the reaction, the reactor was cooled to room temperature and the reaction mixture was diluted with acetone (20 cm^3) and filtered via a syringe filter (0.1 μm). An aliquot of this solution was mixed with a GC calibration solvent nonane and then analyzed with a Younglin YL6500 gas chromatograph (GC) equipped with a FID detector and a HP-5 column (30 m × 0.32 mm × 0.25 μm). More detailed GC analysis was done in an Agilent Technologies 7890 A GC equipped with an auto sampler (7683D), a flame ionization detector (FID) and a Restek Rxi®-17Sil column (30 m × 0.25 mm × 0.25 μm). The conversion of H_{12}-MBP and the selectivities to H_6-MBP and H_0-MBP were calculated from the quantities of the reactant consumed and the products formed, using the calibration factors calculated quantitatively from the calibration curves of three authentic samples.

The aforementioned procedure was applied for H_2 release from different substrates such as H_{12}-NEC (7.24 mmol), octahydroindole (9.74 mmol), decahydroquinoline (10.83 mmol), perhydro 2-methyl-6-(n-methylbenzyl)pyridine (8.6 mmol) and perhydro 2-methylindole (10.77 mmol).

Catalyst stability test. Based on the steps taken in our previous study[25], the catalyst sample recovered after the reaction was washed three times with a mixture of acetone and heptane and dried at 105 °C in an oven. As a final step, the sample was reduced by H_2 at 350 °C for 3 h. This procedure was repeated after each reaction run.

Data availability
The authors declare that the data supporting the findings of this study are available within the article and its Supplementary Information files. All other relevant data are available from the authors on reasonable request.

References
1. Hu, P., Fogler, E., Posner, Y. D., Iron, M. A. & Milstein, D. A novel liquid organic hydrogen carrier system based on catalytic peptide formation and hydrogenation. *Nat. Commun.* **6**, 6859 (2015).
2. Turner, J. A. Sustainable hydrogen production. *Science* **305**, 972–974 (2004).
3. Sotoodeh, F. & Smith, K. J. Structure sensitivity of dodecahydro-N-ethylcarbazole dehydrogenation over Pd catalysts. *J. Catal.* **279**, 36–47 (2011).
4. Zhu, Q. L. & Xu, Q. Liquid organic and inorganic chemical hydrides for high-capacity hydrogen storage. *Energy Environ. Sci.* **8**, 478–512 (2015).
5. Sotoodeh, F. & Smith, K. J. Analysis of H_2 release from organic polycyclics over Pd catalysts using DFT. *J. Phys. Chem. C.* **117**, 194–204 (2013).
6. Oh, J. et al. 2-(N-Methylbenzyl)pyridine: a potential liquid organic hydrogen carrier with fast H_2 release and stable activity in consecutive cycles. *ChemSusChem* **11**, 661–665 (2018).
7. Bachmann, P. et al. Dehydrogenation of the liquid organic hydrogen carrier system indole/indoline/octahydroindole on Pt(111). *J. Phys. Chem. C.* **122**, 4470–4479 (2018).
8. Teichmann, D. et al. Energy storage in residential and commercial buildings via liquid organic hydrogen carriers (LOHC). *Energy Environ. Sci.* **5**, 9044–9054 (2012).
9. Stark, K. et al. Liquid organic hydrogen carriers: thermophysical and thermochemical studies of carbazole partly and fully hydrogenated derivatives. *Ind. Eng. Chem. Res.* **54**, 7953–7966 (2015).
10. Amende, M. et al. Size and structure effects controlling the stability of the liquid organic hydrogen carrier dodecahydro-N-ethylcarbazole during dehydrogenation over Pt model catalysts. *J. Phys. Chem. Lett.* **5**, 1498–1504 (2014).
11. Amende, M. et al. Model catalytic studies of liquid organic hydrogen carriers: dehydrogenation and decomposition mechanisms of dodecahydro-N-ethylcarbazole on Pt(111). *ACS Catal.* **4**, 657–665 (2014).
12. Do, G. et al. Hydrogenation of the liquid organic hydrogen carrier compound dibenzyltoluene—reaction pathway determination by ^{1}H NMR spectroscopy. *React. Chem. Eng.* **1**, 313–320 (2016).
13. Emel'yanenko, V. N. et al. Hydrogen storage: thermochemical studies of N-alkylcarbazoles and their derivatives as a potential liquid organic hydrogen carriers. *J. Phys. Chem. C.* **119**, 26381–26389 (2015).
14. Jorschick, H. et al. Hydrogen storage using a hot pressure swing reactor. *Energy Environ. Sci.* **10**, 1652–1659 (2017).
15. Espinosa, D. V., Beltran, A. M. & Mata, J. A. Catalytic hydrogen production by ruthenium complexes from the conversion of primary amines to nitriles: potential application as a liquid organic hydrogen carrier. *Chem. Eur. J.* **22**, 17758–17766 (2016).
16. He, T., Pei, Q. & Chen, P. Liquid organic hydrogen carriers. *J. Energy Chem.* **24**, 587–594 (2015).
17. Muller, K. et al. Liquid organic hydrogen carriers: thermophysical and thermochemical studies of benzyl- and dibenzyl-toluene derivatives. *Ind. Eng. Chem. Res.* **54**, 7967–7976 (2015).
18. Schildhauer, T., Newson, E. & Muller, S. The equilibrium constant for the methylcyclohexane–toluene system. *J. Catal.* **198**, 355–358 (2001).
19. Crabtree, R. H. Hydrogen storage in liquid organic heterocycles. *Energy Environ. Sci.* **1**, 134–138 (2008).
20. Pez, G. P., Scott, A. R., Cooper, A. C. & Cheng, H. Hydrogen storage by reversible hydrogenation of pi-conjugated substrates. US Patent 7101530B2 (2006).
21. Clot, E., Eisenstein, O. & Crabtree, R. H. Computational structure–activity relationships in H_2 storage: how placement of N atoms affects release

temperatures in organic liquid storage materials. *Chem. Commun.* 2231–2233 (2007). https://pubs.rsc.org/en/content/articlelanding/2007/cc/b705037b#!divAbstract.

22. Markiewicz, M. et al. Environmental and health impact assessment of liquid organic hydrogen carrier (LOHC) systems—challenges and preliminary results. *Energy Environ. Sci.* **8**, 1035–1045 (2015).

23. Dong, Y., Yang, M., Yang, Z., Ke, H. & Cheng, H. Catalytic hydrogenation and dehydrogenation of N-ethylindole as a new heteroaromatic liquid organic hydrogen carrier. *Int. J. Hydrog. Energy* **40**, 10918–10922 (2015).

24. Li, L., Yang, M., Dong, Y., Mei, P. & Cheng, H. Hydrogen storage and release from a new promising liquid organic hydrogen storage carrier (LOHC): 2-Methylindole. *Int. J. Hydrog. Energy* **41**, 16129–16134 (2016).

25. Oh, J., Kim, T. W., Jeong, K., Park, J. H. & Suh, Y. W. Enhanced activity and stability of a carbon-coated alumina-supported Pd catalyst in the dehydrogenation of a liquid organic hydrogen carrier, perhydro 2-(*n*-methylbenzyl)pyridine. *ChemCatChem* **10**, 3892–3900 (2018).

26. Sobota, M. et al. Dehydrogenation of dodecahydro-N-ethylcarbazole on Pd/Al$_2$O$_3$ model catalysts. *Chem. Eur. J.* **17**, 11542–11552 (2011).

27. Amende, M. et al. Dehydrogenation mechanism of liquid organic hydrogen carriers: dodecahydro-N-ethylcarbazole on Pd(111). *Chem. Eur. J.* **19**, 10854–10865 (2013).

28. Bartholomew, C. H., Woodfield, B. F., Huang, B., Olsen, R. E. & Astle, L. Method for making highly porous, stable metal oxides with a controlled pore structure. US Patent 0257008A1 (2011).

29. Huang, B., Bartholomew, C. H., Smith, S. J. & Woodfield, B. F. Facile solvent-deficient synthesis of mesoporous γ-alumina with controlled pore structures. *Micro Meso. Mater.* **165**, 70–78 (2013).

30. Brunner, K. M., Huang, B., Woodfield, B. F. & Hecker, W. C. Iron Fischer-Tropsch catalysts prepared by solvent-deficient precipitation (SDP): Effects of washing, promoter addition step, and drying temperature. *Catalysts* **5**, 1352–1374 (2015).

31. Brunner, K. M. et al. Preparation of an unsupported iron Fischer-Tropsch catalyst by a simple, novel, solvent-deficient precipitation (SDP) method. *Energy Fuels* **29**, 1972–1977 (2015).

32. Albretsen, M. K. et al. Effect of drying temperature on iron Fischer-Tropsch catalysts prepared by solvent deficient precipitation. *J. Nanomaterials* **2017**, 1–11 (2017).

33. Sepehri, S., Rezaei, M., Garbarino, G. & Busca, G. Facile synthesis of a mesoporous alumina and its application as a support of Ni-based autothermal reforming catalysts. *Int. J. Hydrog. Energy* **41**, 3456–3464 (2016).

34. Sepehri, S., Rezaei, M., Garbarino, G. & Busca, G. Preparation and characterization of mesoporous nanocrystalline La-, Ce-, Zr-, Sr-containing Ni-Al$_2$O$_3$ methane autothermal reforming catalysts. *Int. J. Hydrog. Energy* **41**, 8855–8862 (2016).

35. Bruckner, N. et al. Evaluation of industrially applied heat-transfer fluids as liquid organic hydrogen carrier systems. *ChemSusChem* **7**, 229–235 (2014).

36. Cui, Y. et al. The effect of substitution on the utility of piperidines and octahydroindoles for reversible hydrogen storage. *New J. Chem.* **32**, 1027–1037 (2008).

37. Saksa, P. T. A., Cook, C., Kiviaho, J. & Repo, T. Liquid organic hydrogen carriers for transportation and storing of renewable energy – Review and discussion. *J. Power Sources* **396**, 803–823 (2018).

38. Bhogeswararao, S. & Srinivas, D. Catalytic conversion of furfural to industrial chemicals over supported Pt and Pd catalysts. *J. Catal.* **327**, 65–77 (2015).

39. Zheng, Q., Farrauto, R. & Deeba, M. Part II: oxidative thermal aging of Pd/Al$_2$O$_3$ and Pd/Ce$_x$O$_y$-ZrO$_2$ in automotive three way catalysts: The effects of fuel shutoff and attempted fuel rich regeneration. *Catalysts* **5**, 1797 (2015).

40. Esteves, L. M., Brijaldo, M. H. & Passos, F. B. Decomposition of acetic acid for hydrogen production over Pd/Al$_2$O$_3$ and Pd/TiO$_2$: Influence of metal precursor. *J. Mol. Catal. A: Chem.* **422**, 275–288 (2016).

41. Smith, S. J. et al. Synthesis of metal oxide nanoparticles via a robust "solvent-deficient" method. *Nanoscale* **7**, 144–156 (2015).

42. Zhu, B. & Jang, B. W. L. Insights into surface properties of non-thermal RF plasmas treated Pd/TiO$_2$ in acetylene hydrogenation. *J. Mol. Catal. A: Chem.* **395**, 137–144 (2014).

43. Fan, Q. et al. Photodeposited Pd nanoparticles with disordered structure for phenylacetylene semihydrogenation. *Sci. Rep.* **7**, 42172 (2017).

44. Feng, H., Lu, J., Stair, P. C. & Elam, J. W. Alumina over-coating on Pd nanoparticle catalysts by atomic layer deposition: Enhanced stability and reactivity. *Catal. Lett.* **141**, 512–517 (2011).

45. Hicks, R. F., Qi, H., Young, M. L. & Lee, R. G. Structure sensitivity of methane oxidation over platinum and palladium. *J. Catal.* **122**, 280–294 (1990).

46. Lear, T., Marshall, R., Sanchez, J. A. L. & Jackson, S. D. The application of infrared spectroscopy to probe the surface morphology of alumina-supported palladium catalysts. *J. Chem. Phys.* **123**, 174706 (2005).

47. Binet, C., Jadi, A., Lavalley, J. C. & Boutonnet-Kizling, M. Metal-support interaction in Pd/CeO$_2$ catalysts: fourier-transform infrared studies of the effects of the reduction temperature and metal loading. *J. Chem. Soc. Faraday Trans.* **88**, 2079–2084 (1992).

48. Tessier, D., Rakai, A. & Bozon-Verduraz, F. Spectroscopic study of the interaction of carbon monoxide with cationic and metallic palladium in palladium-alumina catalysts. *J. Chem. Soc. Faraday Trans.* **88**, 741–749 (1992).

Acknowledgements

Author contributions

J.O.: catalyst characterization, catalytic experiments, and contributed to manuscript writing and revision. H.B.B.: material design, synthesis, characterization, and contributed to manuscript writing and revision. J.H.P.: Starting material synthesis, design and direction of the project, contributed to manuscript writing. Y-W.S.: Design and direction of the project, conceived and supervised the project, and wrote and revised the manuscript.

Additional information

Supplementary information accompanies this paper at https://doi.org/10.1038/s42004-019-0167-7.

Competing interests: The authors declare no competing interests.

Reprints and permission information is available online at http://npg.nature.com/reprintsandpermissions/

Publisher's note: Springer Nature remains neutral with regard to jurisdictional claims in published maps and institutional affiliations.